NICKEL HYDROXIDE CORROSION RESIDUES ON METALLIZED Ni/Au CERAMIC PACKAGES

Minerva M. Cruz and Russell T. Winslow
Six Sigma
Milpitas, CA, USA
minerva@solderquik.com

ABSTRACT
This study focuses on identifying the residues found on the surface of high temperature co-fired ceramic packages after prolonged exposure to moisture. Using a "farming method", enough residue was created to facilitate a thorough analysis. Tests using SEM-EDS, Fourier Transform Infrared Spectroscopy, Raman Spectroscopy, and X-ray Diffraction have identified these residues as primarily β-$Ni(OH)_2$ and α-$Ni(OH)_2$. Traces of tungsten oxide and a silicate compound were also detected.

The findings of this study should help process engineers resolve package-related problems when nickel-gold finishes are utilized. It may also help explain why pure gold finishes fail solderability testing after steam-conditioning -- a test they should otherwise pass with ease.

Key words: Nickel Hydroxide, Solderability, HTCC, Corrosion

INTRODUCTION

High-temperature co-fired ceramic (HTCC) substrates are commonly used for packaging integrated circuits for high-reliability, industrial, military, and aerospace applications. The most common HTCC substrates are built with a refractory metal (e.g., tungsten or molybdenum), which is printed on the precursor ceramics prior to firing. After co-firing, the refractory metal is cleaned and plated with nickel and then gold. The nickel provides a basis metal for the future solder joint and the gold provides for corrosion protection throughout the assembly process. This gold layer must be thick enough in order to protect the underlying metallization during subsequent package assembly processes such as die attach, lid seal, burn-in, etc. In fact, MIL-PRF-38535 requires that these packages have a minimum of 1.27 µm of gold [1]. Because of the propensity for gold to cause solder joint embrittlement, the gold is typically removed and replaced with solder prior to board mounting. Hot solder dip is typically employed to remove this gold and the pads are left coated with Sn63-Pb37 solder.

During the hot solder dip process, solderability problems were encountered. Conventional wisdom has attributed this to the diffusion of oxygen, through the porous gold finish, and the subsequent oxidation of the underlying nickel layer. To avoid this problem, many companies use pure nitrogen in all high-temperature operations such as lid seal and burn-in. However, recent studies have shown that moisture plays a more important role in the degradation of the solderability of these packages [2].

For several years now, solderability issues have been occasionally found on metallized Ni/Au ceramic packages, such as land grid arrays (LGAs). Similar concerns on leadless chip carrier (LCC) packages have been reported almost 20 years ago [3]. These solderability issues were found not only on steam-conditioned packages, but also on packages that were not subjected to accelerated aging. An example of a LGA with non-wetting and dewetting is shown in Figure 1.

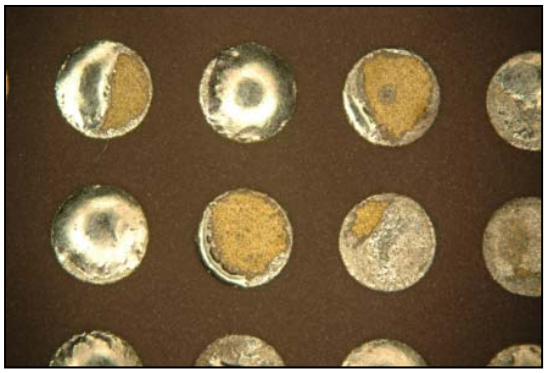

Figure 1. Solderability issues (non-wetting and dewetting) on a LGA in a production lot.

Another issue that is intermittently encountered is the presence of a white residue (commonly known as "white crud") in the castellations of LCCs, as shown in Figure 2. This white residue is commonly found when the packages have been subjected to prolonged exposure to moisture.

Figure 2. White residue in LCC castellations.

A study was conducted by the authors in 2010 to attempt to prove that thin gold, together with high temperature assembly operations (in air), such as lid seal and burn-in, were the root cause of these solderability failures. The purpose of the study was to evaluate the effects of high temperature and steam-conditioning on the solderability of Ni/Au ceramic packages such as LGAs and LCCs. In that study, two types of samples were used – one type with thin Au (~ 0.1 µm) and another with thick Au (~ 4 µm). These sample types were divided into two groups, with one set of thin Au samples merged with one set of thick Au. One set was subjected to simulated lid seal at 340°C (~7 minute reflow) and burn-in at 175°C for 2 weeks, while the other set was steam-conditioned for 8 hours at 93°C.

After steam-conditioning, dip and look solderability test was conducted in accordance with MIL-STD-883 Method 2003 [4]. The samples that had the simulated lid seal and burn-in all passed dip and look solderability test. However, those that were steam-conditioned at 93°C for 8 hours all failed solderability testing. In fact, these samples failed even after only 1 hour of steam-conditioning. From that study, it was concluded that steam-conditioning, and not high-temperature, is what destroys the solderability of these packages.

Upon closer examination of packages that failed solderability testing, an almost non-detectable residue on the surface of the Ni/Au metallization was found. The picture shown in Figure 3 is a typical example of the residue found on packages that were steam-conditioned for 8 hours before the dip and look test. This residue was characterized using X-ray Photoelectron Spectroscopy (XPS) and Fourier Transform Infrared Spectroscopy (FTIR). The XPS results indicated the presence of Ni^{2+} and O^{2-}, with a 1:2 atomic ratio. The FTIR results showed strong peaks of O-H bands, which was attributed to an inorganic compound. It was very difficult to ascertain the exact composition of the residue that has been causing these solderability issues. This is because XPS only provides the chemical state of an element (e.g., Ni^{+} versus Ni^{2+}), while FTIR, even though it is good at identifying organic functional groups, provides limited information on inorganic compounds. Hence, a method needed to be created to enhance the formation of this residue so that it can be analyzed thoroughly.

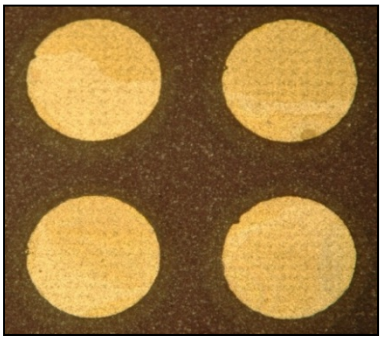

Figure 3. Residue on Ni/Au ceramic packages.

In this study, a "farming method" was developed to maximize this residue. A thorough analysis of this residue, which is assumed to be a corrosion by-product, that forms on the surface of the Au layer and that prevents the wetting and spreading of the solder, is also presented.

EXPERIMENTAL METHODOLOGY

Experimental Procedure

In a previous study, it was shown that moisture and not heat is what destroys the solderability of Ni/Au metallized ceramic LGA and LCC pads [2]. The residue that causes this solderability failure is very difficult to detect even after 8 hours of steam-conditioning at 93°C. In order to thoroughly understand the nature of this residue, a "farming method" was developed. To accomplish this, the die attach pads of Ni/Au metallized LGAs and LCCs were scratched and then steam-conditioned for 168 hours.

Shown in Table 1 are the substrate types used for this study. Ten samples each were used for Sets 1, 3 and 4, while only five samples were used for Set 2.

Table 1. Substrates showing supplier, manufacture date, and metallization.

Set	Supplier	Date	Layer 1	Layer 2	Layer 3
1	A	1987	W[1]	Ni[2]	Au[2]
2	A	2001	Mo[1]	Ni-B[3]	Au[3]
3	B	1990	W[1]	Ni[2]	Au[2]
4	B	2010	W[1]	Ni-B[3]	Au[4]

Note: [1]Screen printed before sintering, [2]Electrolytic plating, [3]Electroless plating, [4] Immersion plating

Characterizations

Scanning Electron Microscopy - Energy Dispersive Spectroscopy (SEM-EDS) was used to determine the microstructure and elemental composition of the residue. Low vacuum was used so there was no need to coat the samples, and an accelerating voltage of 25 kV was used.

Fourier Transform Infrared Spectroscopy (FTIR) was utilized to determine the chemical bonding and molecular structure of the residue. The residue was transferred to an infrared transmitting substrate and analyzed using the FTIR microscope in transmission mode.

Raman spectroscopy was also used to determine the chemical structure of the residue. An Ar^{+} ion laser (514.5 nm wavelength), an 1800 gr/mm grating, and backscattering geometry (180°) were used for the measurements.

Micro X-ray diffraction (XRD) was used to determine the crystal structure of the residue. A small amount of residue was mounted to the end of a glass capillary. The capillary was placed in a goniometer head with x-y-z motion for analysis. Data was acquired on a micro-diffractometer equipped with a copper x-ray tube with a wavelength of 1.54059Å, incident-beam monochromator, 500 µm pinhole collimator, laser alignment system, and 2D detector. 2D data was acquired with the detector positioned at 2θ values of 12˚, 26˚, 42˚, and 60˚.

RESULTS AND DISCUSSION

Typical examples of the SEM images, EDS, FTIR, Raman, and XRD spectra are shown in the figures below.

An SEM image and corresponding EDS spectrum of the residue are shown in Figures 4 and 5. Strong peaks of Ni, O, W, and Au were seen. Si, Al, Ca, and Mg peaks, from the ceramic substrate were also found.

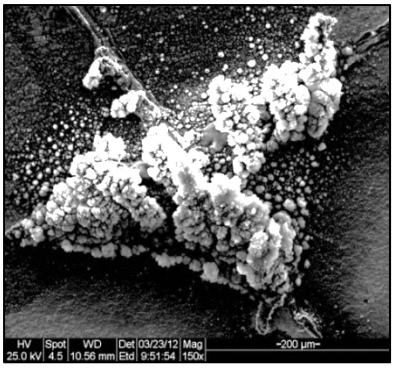

Figure 4. SEM image of the residue.

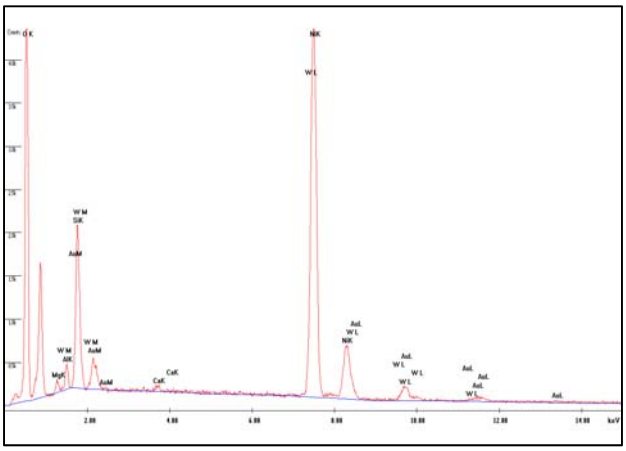

Figure 5. EDS spectrum of the residue shown in Figure 4.

Shown in Figure 6 are high-magnification SEM micrographs of the residue. The cauliflower-shaped morphology and network-like microstructure is consistent with the flower-shaped β-$Ni(OH)_2$ found by Al-Hajry *et al.* [5]; however, the cauliflower-shaped microstructures found in this study (shown in Figure 6a) are bigger in diameter than the ones found in that work (~20 µm versus 3-5 µm). This size difference may be attributed to the "farming method", in that the residues were "forced" to grow, hence, their larger size, while those found in the literature were prepared from limited amounts of aqueous solutions.

The nanosheets that compose the network-like structure (shown in Figure 6b) are also longer (~5 µm versus 1.5-2 µm). $Ni(OH)_2$ has a tendency to form a 2D lamellar structure. These lamellar structures are thermodynamically stable along the c-axis direction, hence, they join together and form the network-like sheets in the flower-shaped structures [6].

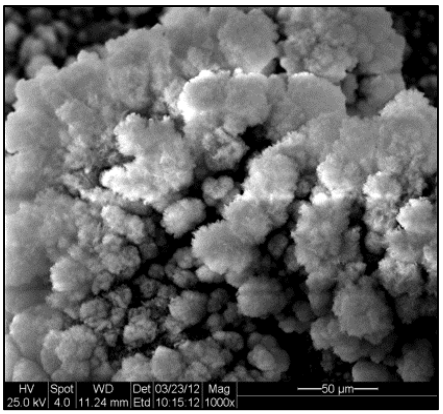

(a)

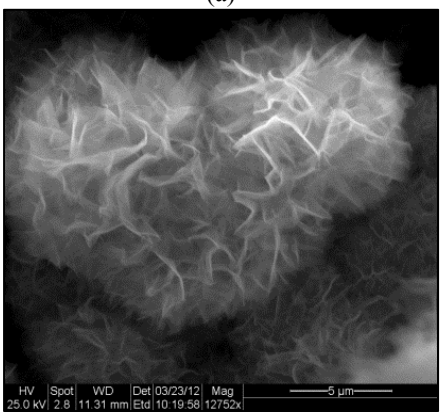

(b)

Figure 6. SEM images of the residue, showing the (a) cauliflower-shaped, and (b) network-like morphology.

An FTIR spectrum of the residue is shown in Figure 7. The sharp and narrow peak at 3642 cm^{-1} is characteristic of the non-hydrogen bonded O-H stretching vibration, and confirms the brucite-like structure of the β-$Ni(OH)_2$ phase, which is similar to those found in the literature [5, 7]. The broad absorption band centered around 3393 cm^{-1} corresponds to the presence of hydrogen bonded O-H group, which is due to a high degree of hydration [8]. The 3393 cm^{-1} peak is typically attributed to the α-$Ni(OH)_2$ phase [9-10]. The peak at 1635 cm^{-1} is attributed to the bending deformation of water molecules [10-11]. The band at 1419 cm^{-1} is due to the in-plane O-H bending [8, 12] and the 847 cm^{-1} peak may probably be due to an O-H out-of-plane deformation. The strong peak at 999 cm^{-1} may be due to an inorganic silicate compound [13].

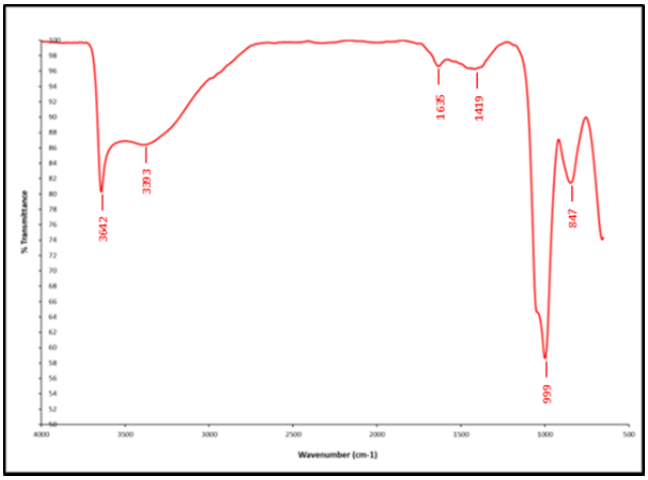

Figure 7. FTIR spectrum of the white residue.

A Raman spectrum is shown in Figure 8. The peak at 334 cm^{-1} is due to the symmetric stretching of the hydroxyl groups, while the peaks at 458 cm^{-1} and 3590 cm^{-1} are due to the Ni-O stretching and an E-type stretching of the Ni-OH lattice, which are all characteristic of the β-$Ni(OH)_2$ phase [14]. The peak at 854 cm^{-1} is probably an O-H stretching band, while the strong peak at 933 cm^{-1} is typically due to an inorganic silicate compound [15]. This inorganic silicate compound is possibly a metal atom with two terminal oxygen atoms, in this case, Si=O [16].

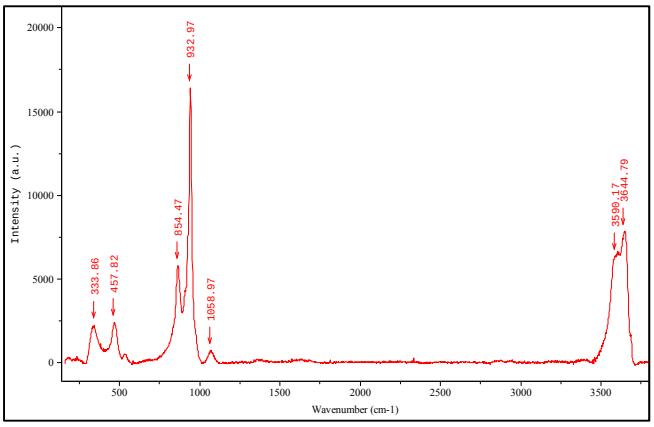

Figure 8. Raman spectrum of the residue.

The crystallinity and crystal structure of the residue was determined using micro-XRD. Unlike traditional point detectors, the 2D detector accepts diffraction from crystallites oriented in a wide variety of tilt angles with respect to the incident x-ray beam. This results in reasonable diffraction intensity even though the sample size is very small. An XRD pattern for the residue is shown in Figure 9. All major diffraction peaks have been indexed as hexagonal β-$Ni(OH)_2$ and match well with the reported standard values (PDF #014-0117 [17]). These peaks are indexed in Figure 9.

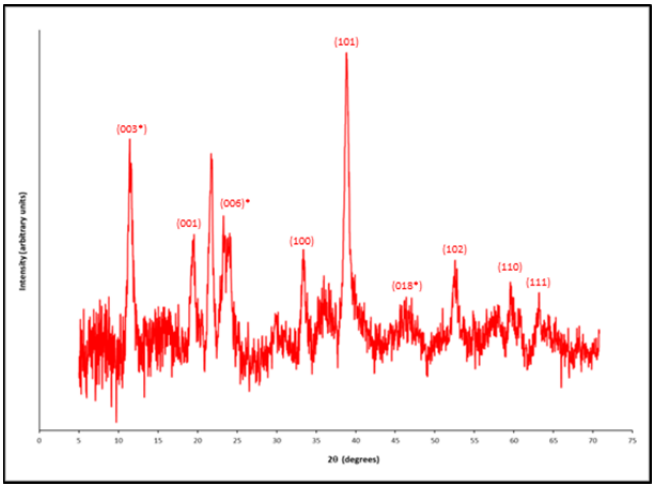

Figure 9. XRD spectrum of the residue.

Shown in Table 2 are the observed interplanar distance spacing, d_{obs}, and the reported standard values for each (hkl) value for β-$Ni(OH)_2$. The values for d_{obs} were calculated using the following Bragg's law equation:

$$d_{obs} = \frac{1.54059\ \text{Å}}{2*\sin(\frac{2\theta}{2})} \qquad \text{Equation 1}$$

Table 2. XRD data for the β-$Ni(OH)_2$ residue.

(hkl)	2θ (˚)	d_{obs} (Å)	d_{std} (Å)
(101)	38.80	2.32	2.30
(001)	19.36	4.58	4.61
(100)	33.36	2.68	2.71
(102)	52.54	1.74	1.75
(110)	59.50	1.55	1.56
(111)	63.16	1.47	1.48

The d_{obs} values match well with d_{std} and strongly shows that the residue is β-$Ni(OH)_2$.

Several remaining peaks were also found on the XRD spectrum. The peaks at 11.40˚, 22.86˚, and 46.12˚ correspond to (003), (006), and (018) planes of the rhombohedral α-$Ni(OH)_2$ and is in good agreement with the reported values (PDF #038-0715 [18]). These peaks are indexed with an asterisk in Figure 9. The d_{obs} values are shown in Table 3. Some of the smaller peaks that were not indexed in Figure 9, but were assigned automatically by the XRD software were included in Table 3. These d_{obs} values were calculated using Equation 1 above.

The other two intense peaks at 21.70˚ and 23.20˚were indexed to be the most intense peaks for silicate hydrate (PDF #038-0448 [19]), and tungsten oxide, WO_3 (PDF #043-1035 [20]). These XRD results correlate very well with those found on the EDS, FTIR, and Raman spectra.

Table 3. XRD data for the α-$Ni(OH)_2$ residue.

(hkl)	2θ (˚)	d_{obs} (Å)	d_{std} (Å)
(003)	11.40	7.76	7.79
(006)	22.86	3.89	3.91
(101)	33.84	2.65	2.68
(015)	38.80	2.32	2.32
(018)	46.12	1.97	1.97

As can be seen from the XRD spectrum in Figure 9, the β-$Ni(OH)_2$ phase has bands that are very narrow, with small FWHM values, which may be due to its high-crystalline nature. On the other hand, α-$Ni(OH)_2$ has a turbostratic nature, which means that it has a less-ordered structure, and this disorder results in broad XRD peaks [10].

The test methodologies utilized above prove that the corrosion residues found on these metallized Ni/Au ceramic packages is primarily nickel hydroxide. Six Sigma has found that this corrosion residue forms a tenacious, adherent film on the Ni/Au metallized surfaces. It is also very difficult to detect when it is very thin, hence, a "farming method" had to be utilized to make it thicker in order to have enough samples for a more complete analysis. Six Sigma has also found that this corrosion residue is not soluble in water and most solvents, and believes that this residue converts to nickel oxide, giving off water in the process. This might help explain the presence of water during Residual Gas Analysis (RGA) testing of hermetic integrated circuits.

CONCLUSION

In this study, the residues found on the surface of gold-plated HTCC substrates, after prolonged exposure to moisture, have been identified. These residues are a mixture consisting primarily of β-$Ni(OH)_2$ and α-$Ni(OH)_2$. Other constituents, which appear to be tungsten oxide and a silicate compound, were also found.

These α-$Ni(OH)_2$ and β-$Ni(OH)_2$ corrosion residues may help explain some issues found in integrated circuit manufacturing and packaging, such as:

- solderability failures
- die attach voids
- variation in wire bond strengths
- lid seal voids

Six Sigma has found that these corrosion residues need to be removed in order to promote good wetting, and hence, maximize board-level reliability.

FUTURE WORK

The corrosion mechanism responsible for the formation of the corrosion by-products, α-$Ni(OH)_2$ and β-$Ni(OH)_2$, needs to be studied. The effects of other factors, such as % relative humidity, chlorine, and sulfur-bearing materials, also need to be explored.

REFERENCES

1. MIL-PRF-38535, Integrated Circuits (Microcircuits) Manufacturing (2013).
2. M. Cruz and R. Winslow, *CGA Pad Solderability*, Procs. Space Parts Working Group Conference, Torrance, CA, 2010.
3. B.D. Dunn, *"Metallurgical Evaluation of Steam Aged LCCC Devices following Solderability Testing,"* Soldering and Surface Mount Technology, **15**, 28-32 (1993).
4. MIL-STD-883 Method 2003, Test Method Standard – Microcircuits (2015).
5. A. Al-Hajry, A. Umar, M. Vaseem, M.S. Al-Assiri, F. El-Tantawy, M. Bououdina, S. Al-Heniti and Y.B. Hahn, *"Low-temperature growth and properties of flower-shaped β-$Ni(OH)_2$ and NiO structures composed of thin nanosheet networks,"* Superlattices and Microstructures (2008).
6. D. Wang, C. Song, Z. Hu, X. Fu, *"Fabrication of Hollow Spheres and Thin Films of Nickel Hydroxide and Nickel Oxide with Hierarchical Structures,"* J. Phys. Chem. B, **109** (3), 1125-1129 (2005).
7. M. Rajamathi, G.N. Subbanna and P.V. Kamath, *"On the existence of a nickel hydroxide phase which is neither α nor β,"* J. Mater. Chem., **7** (11), 2293-2296 (1997).
8. G. Socrates, Infrared and Raman Characteristic Group Frequencies, 3rd ed. (John Wiley & Sons Ltd Press. Chichester, England, 2001), pp. 95.
9. R. Acharya, T. Subbaiah, S. Anand and R.P. Das, *"Preparation, characterization and electrolytic behavior of β-nickel hydroxide,"* J. Power Sources, 109, 494-499 (2002).
10. G. Fu, Z. Hu, L. Xie, X. Jin, Y. Xie, Y. Wang, Z. Zhang, Y. Yang and H. Wu, *"Electrodeposition of nickel hydroxide films nickel foil and its electrochemical performances for supercapacitor,"* Int. J. Electrochem. Sci., 4, 1052-1062 (2009).
11. M.K. Motlagh, A. Youzbashi and L. Sabaghzadeh, *"Synthesis and characterization of nickel hydroxide/oxide nanoparticles by the complexation-precipitation method,"* Int. J. Phys. Sci., **6** (6), 1471-1476 (2011).
12. B. Smith, Infrared Spectral Interpretation: A Systematic Approach (CRC Press. Boca Raton, Florida, 1999), pp. 245.
13. G. Socrates, *op. cit.,* pp. 291.
14. C. Liu and Y. Li, *"Synthesis and characterization of amorphous α-nickel hydroxide,"* J. Alloys and Comp., 478, 415-418 (2009).
15. G. Socrates, *op. cit.,* pp. 245.
16. G. Socrates, *op. cit.,* pp. 327.
17. The International Center for Diffraction Data, Swathmore, PA, *PDF #014-0117*.
18. The International Center for Diffraction Data, Swathmore, PA, *PDF #038-0715*.
19. The International Center for Diffraction Data, Swathmore, PA, *PDF #038-0448*.
20. The International Center for Diffraction Data, Swathmore, PA, *PDF #043-1035*.